Available online at www.sciencedirect.com
ScienceDirect
C. R. Physique 9 (2008) 550–569
COMPTES RENDUS PHYSIQUE
http://france.elsevier.com/direct/COMREN/

Synchrotron x-rays and condensed matter/Rayonnement X synchrotron et matière condensée

Magnetic and resonant X-ray scattering investigations of strongly correlated electron systems

Luigi Paolasini *, François de Bergevin

European Synchrotron Radiation Facility, 6, rue Jules-Horowitz, boîte postale 220, 38043 Grenoble cedex, France

Available online 25 October 2007

Abstract

Resonant X-ray scattering is a method which combines high-$\vec{Q}$ resolution X-ray elastic diffraction and atomic core-hole spectroscopy for investigating electronic and magnetic long-range ordered structures in condensed matter. During recent years the development of theoretical models to describe resonant X-ray scattering amplitudes and the evolution of experimental techniques, which include the control and analysis of linear photon polarization and the introduction of extreme environment conditions such as low temperatures, high magnetic field and high pressures, have opened a new field of investigation in the domain of strongly correlated electron systems. ***To cite this article: L. Paolasini, F. de Bergevin, C. R. Physique 9 (2008).***
© 2007 Académie des sciences. Published by Elsevier Masson SAS. All rights reserved.

Résumé

Étude de systèmes électroniques fortement corrélés par diffusion magnétique et résonnante des rayons X. La méthode de diffusion résonnante des rayons X combine la diffraction à haute résolution en $\vec{Q}$ avec la spectroscopie des niveaux atomiques de cœur. Elle permet l'étude, dans la matière condensée, des structures électroniques et magnétiques ordonnées à grande distance. Les dernières années ont vu le développement de modèles théoriques décrivant les amplitudes de diffusion résonante des rayons X, et une évolution des techniques expérimentales incluant le contrôle et l'analyse de la polarisation linéaire des photons et l'introduction d'environnements extrêmes tels que basses températures, champ magnétiques élevés et hautes pressions. Ces développements théoriques et expérimentaux ont ouvert un nouveau champ d'investigation dans le domaine des systèmes électroniques fortement corrélés. ***Pour citer cet article : L. Paolasini, F. de Bergevin, C. R. Physique 9 (2008).***
© 2007 Académie des sciences. Published by Elsevier Masson SAS. All rights reserved.

Keywords: Resonant X-ray scattering; Strongly correlated electron systems

Mots-clés : Diffusion résonnante des rayons X ; Systèmes électroniques fortement corrélés

1. Introduction

The use of photon beam techniques to study the magnetic properties of materials has received a large impulse with the advent of the so-called third generation synchrotron radiation sources. The improvement in brightness, polarization and energy tunability of the light delivered by the insertion devices (wigglers and undulators) have been

* Corresponding author.
E-mail address: paolasin@esrf.fr (L. Paolasini).

1631-0705/$ – see front matter © 2007 Académie des sciences. Published by Elsevier Masson SAS. All rights reserved.
doi:10.1016/j.crhy.2007.06.005

key ingredients for a wide range of applications of synchrotron radiation in many diverse areas of condensed matter, including physics, chemistry, material science, biology, medicine, geology. The research field of Resonant X-ray Scattering (RXS) has experienced tremendous theoretical and experimental progress during the last years, and today it is one of the most important areas of investigation of modern synchrotron radiation sources [1]. This method uses the photon beam as a quantum probe to investigate structural, magnetic and electronic ordered structures of solids, and combines high-$\vec{Q}$ resolution X-ray diffraction and atomic spectroscopy for investigating the subtleties of microscopic electronic and magnetic interactions in solids.

The fundamental idea of RXS is that the incident photon energy, tuned across an absorption edge, is sufficient to cause a core-level electron to be injected to a partially filled valence band shell and to subsequently decay through the emission of an elastically scattered photon with a particular polarization dependence. Whereas the pure X-ray magnetic scattering amplitude is very weak, and enables the separation of spin and orbital moment contributions to the total magnetization density without any underlying models [2], large enhancements of the resonant magnetic scattering amplitudes can be found tuning the incident photon energy at L-edge of rare earths or at M-edge of actinides [3]. The special nature of this process is that it is both electron shell and element specific, and it has introduced species sensitivity directly into the determination of magnetic structures.

A feature of the resonant enhancement is the tensor character of atomic structure factors near the absorption edge which reflect the anisotropy of the electronic shells: low site symmetry, Jahn–Teller distortion, local magnetization or electronic orbital order. Due to the tensorial character of the RXS cross-section, superlattice diffraction peaks, forbidden for the space group symmetries, would appear originating from the occurrence of the long range ordering of any physical quantity coupled with the electronic density of states. Similar to the photon spectroscopy, the light polarization is strongly influenced by small changes of local site electronic symmetries, and the polarization analysis of the scattered photons as a function of the incident energy and the sample orientation is the method to unravel the physics that is at the origin of the resonant signals.

Today the RXS technique is particularly active in the research domain of strongly correlated electron systems, in which the electronic correlations play a dominant role, promoting structural, magnetic and electronic phase transitions, driven by a variety of external thermodynamical parameters such as the magnetic field, electric field, high pressure and temperature. The investigation of the order parameters and their evolution as a function of the thermodynamical variables is one of the main research field in the domain of strongly correlated electron systems and complex materials, in which different and often competing order parameters are present, giving rise to many spectacular manifestations of quantum physics in condensed matter. Strongly correlated systems are also a challenge for theoretical models that aim to calculate the electronic structure as it is necessary to correctly treat electron–electron interactions.

Several scattering techniques such as neutrons, X-rays, muons or electrons are exploited to investigate the structure of materials, static and dynamic electronic correlations and collective excitations. Neutrons have occupied an important role in the studies of magnetism in condensed matter for the last fifty years. The evolution of X-ray scattering techniques and the advance in theoretical interpretation of resonant X-ray spectroscopies make synchrotron radiation studies at the forefront of the modern scattering techniques.

2. Historical view

The coupling between magnetism and photons was predicted many years ago, with the observation of important modifications of the Thomson scattering cross-section at high scattering vectors, and this effect is included in the Klein–Nishina formula for Compton scattering [4,5]. In the 1950s different works on Compton magnetic γ-ray scattering were published, motivated by its use for polarization measurements in nuclear and particle physics [6–8]. In the field of solid state physics, seminal and pre-synchrotron magnetic X-ray scattering experiments were carried out in the 1970s by de Bergevin and Brunel at the CNRS in Grenoble, and they demonstrated the feasibility of magnetic X-ray scattering experiments by using a standard X-ray tube on NiO [9], suggested by the theoretical paper of Platzman and Tzoar [10]. The non-resonant limit is well described by these authors in the classical description of the interaction of linearly polarized photons with an electron, as shown in Fig. 1 [11]. A plane wave with a linear polarization $\hat{\epsilon}$ interacts with an electron not only with the charge density as in the case of the Thomson scattering mechanism, but also with the spin and orbital magnetic density of the electrons. The electromagnetic field of the radiation acts as a driving force on the electronic charge which is accelerated with its magnetic moment. The light is re-emitted with a polarization $\hat{\epsilon}'$ after the collision, and the re-radiation mechanisms can be classified as shown in Fig. 1. Beside the

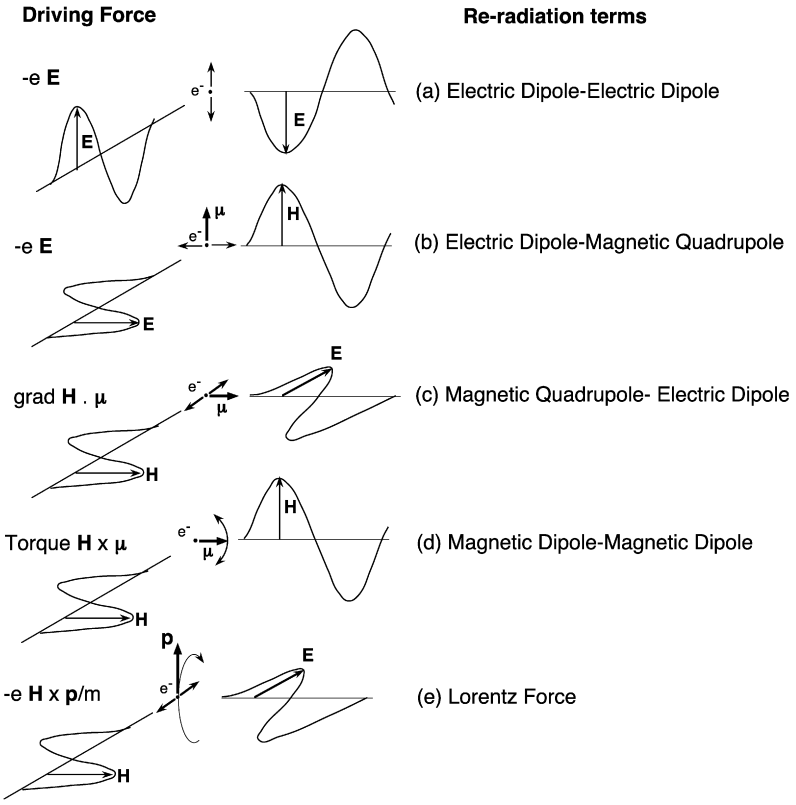

Fig. 1. Classical representation of the dominant scattering mechanisms of the photon–electron interaction [11].

Fig. 1. Représentation en théorie classique des principaux mécanismes d'interaction photon–électron [11].

dominant Thomson term (a), associated to the dipole re-radiation of the scattered field with a classical dependence of the polarization $(\hat{\epsilon} \cdot \hat{\epsilon}')$, the electric and magnetic fields of the radiation interact also with the magnetic moment of the oscillating electron, emitting the magnetic quadrupole (term (b) in Fig. 1). The term (c) corresponds to the interaction between the spin moment of the electron and the magnetic field H of the radiation. The term (d) is associated to the precession of the electronic spin moment which re-radiate a magnetic dipole. Finally the last term (e) corresponds to the correction to the Thomson scattering when the electron has a translational motion, which gives rise to a scattering by orbital moment when integrated over its orbit.

These terms, in general, are very weak, because the relativistic character of the electron–photon interaction introduces a scale factor $(\hbar Q)/(2\pi mc) = 2(\lambda_c/\lambda)\sin\theta$ between the magnetic scattering and the Thomson scattering amplitudes, respectively, where here λ_c is the Compton wavelength of the electron ($\lambda_c = 2\hbar/mc = 0.002426$ nm). Compared to the classical charge scattering the pure magnetic scattering amplitude is significantly reduced by a factor of $\hbar\omega/mc^2$:

$$\frac{\sigma_{\text{mag}}}{\sigma_{\text{charge}}} \simeq \left(\frac{\hbar\omega}{mc^2}\right)^2 \left(\frac{N_m}{N}\right)^2 \langle M\rangle^2 \left(\frac{f_m}{f}\right)^2 \tag{1}$$

where $mc^2 = 511$ keV is the rest mass of an electron, N_m is the number of magnetic electrons per atom and N the number of electrons per atom. $\langle M\rangle$ is the magnetic order parameter, being equal to one only at low temperature, when the system is magnetically saturated (f_m and f are the magnetic and charge form factors). For example, this ratio becomes $\frac{\sigma_{\text{mag}}}{\sigma_{\text{charge}}} \sim 10^{-6}$ for the Mn^{+2} ion (assuming that $f_m/f \sim 1$).

The advent of energy-tunable synchrotron sources has opened the possibility to adjust the photon energy to different values of absorption edges, living the opportunity of observing resonant effects in many materials [12]. These experiments have opened the avenue for the modern synchrotron radiation experiments, allowing the extraction of information from the anisotropic tensors of the atomic structure factor near a resonance: the energy dependence, the

Table 1
Photoabsorption edges for different series of magnetic elements, with the characteristic energy ranges (keV), wavelength λ (Å) and the allowed atomic transitions to the electronic shells. The right column indicates the estimated resonant magnetic scattering amplitudes expressed in r_0 units. The non-resonant pre-factor $\hbar\omega/mc^2$ in Eq. (1) is typically 0.01 r_0

Tableau 1
Table montrant les seuils d'absorption pour diverses séries d'éléments magnétiques, avec les domaines d'énergie caractéristiques (keV), les longueurs d'onde λ (Å) et les transitions permises entre couches atomiques. La colonne de droite indique l'amplitude de diffusion magnétique résonante estimée, exprimée en unités r_0. Le préfacteur non résonant $\hbar\omega/mc^2$ dans l'Éq. (1) vaut typiquement 0,01 r_0

Series	Abs. edge	Energy (keV)	λ (Å)	Shells	Type	Resonant amplitude
3d	$L_{2,3}$	*0.4–1.0*	*12–30*	*2p → 3d*	*E1*	≈ *1.00*
	K	4.5–9.5	1.3–2.7	1s → 4p	E1	≈ 0.02
				1s → 3d	E2	≈ 0.01
5d	$\mathbf{L}_{2,3}$	5.4–14	0.9–2.2	*2p → 5d*	E1	≈ 1.00
4f	$\mathbf{L}_{2,3}$	5.7–10.3	1.2–2.2	2p → 5d	E1	≈ 0.10
				2p → 4f	E2	≈ 0.05
	$M_{4,5}$	*0.9–1.6*	*7.7–13.8*	*2d → 4f*	*E1*	≈ *100*
5f	$\mathbf{L}_{2,3}$	17–21	0.6–0.7	2p → 6d	E1	≈ 0.05
				2p → 4f	E2	≈ 0.01
	$\mathbf{M}_{4,5}$	3.5–4.5	2.7–6	3d → 5f	E1	≈ 10.0

azimuthal rotation and the polarization analysis of the forbidden lattice reflections, appear as a consequence of broken lattice symmetries, as, for example, due to the presence of screw-axis or glide plane broken symmetries [13].

The first resonant magnetic enhancement was reported by Namikawa et al. [14], working at the K-edge of ferromagnetic Ni. In addition to the non-resonant magnetic signal, the authors observed at photon energies close to the K-edge a supplementary signal, which they also interpreted to be of magnetic origin. Since then, the X-ray magnetic circular dichroism is widely used to study ferromagnetic systems. Namikawa's result remained unnoticed until 1988, when Gibbs et al. observed the first resonant enhancement in an antiferromagnetic system [3]. At the L_3-edge of Ho they measured a 50 fold enhancement of the magnetic intensity, explained by the theoretical paper of Hannon et al. [15]. During the 1990s a large number of experiments was performed on magnetic materials, showing large magnetic enhancement at L-edges of rare earths, M-edges of actinides and K-edges of transition metals. The experimental characterization of magnetic resonances and the contiguous theoretical development of the RXS theories have opened with the advent of new beamlines dedicated to RXS studies which today progress in combination with a growing number of experimentalists and theoreticians.

Table 1 shows the absorption edges exploited for RXS studies and associated to the elements of interest for magnetic diffraction. The lines in italic represent absorption edges in the soft X-ray regime, where the scattering conditions are not fulfilled for most of the ordered magnetic structures, but with a huge enhancement of the resonant magnetic amplitude, as shown in the last column (L-edges of transition metals and M-edges of rare earths). The most important edges for hard RXS cover the energy range 3.5–15 keV, which include K-edges of transition metals, the L-edges of Rare-Earths and both the L-edges and the M-edges of actinides. Following the Hannon model for resonant exchange scattering [15], two possible photoelectron transitions are considered in the RXS regime: the electric dipole (E1) and the electric quadrupole (E2) transitions, which are related to the symmetry of the electronic shell and to the type of orbitals probed in the intermediate states. The last column of Table 1 shows the estimation of the magnetic scattering amplitude for the different shells [16]. Notice the strong enhancement at M-edges of rare earths and actinides, arising from the asymmetry of the transition probabilities coupled with the spin-orbit splitting either in the ground state or in the intermediate states, as we will see in the following section.

During the last years, the possibility to single out structural, magnetic and anomalous scattering components through Bragg diffraction, and to study the polarization dependence of the diffracted beam as a function of scattering angles and incident photon energy has provided a large amount of experimental data, that in turn have stimulated theoretical calculations and interpretations. In particular, the Hannon model, valid when a spherical symmetry is broken by an axial vector which determine the magnetic moment, has demonstrated its limitation in the case of strongly correlated electron systems. The discovery of forbidden lattice reflections on V_2O_3 is one of the examples [17] which today still promotes an intense debate on the origin of resonant effects at K-edge of transition metals [18,19], and the

necessity of classifying the high-order multipole resonances taking into account of mixing effects due to parity and time-reversal breaking symmetries. Today, the separation of the RXS signal in terms of electromagnetic multipoles is one of the most fashionable ways to classify these experiments and opens new perspectives in this research field [20–22]. Due to the relatively new domain of research and the complexity of the RXS cross-sections, sophisticated equipment and complex measurements are necessary to disentangle the high-order multipole resonances and to assign the correct character of order parameters involved in the phase transitions. In the following section we will summarize the main theoretical development in this field during the last years, suggesting new experimental investigations and highlighting the role of RXS as the tools to investigate the physics of strongly correlated electron systems.

3. Theory of magnetic and resonant X-ray scattering

The fundamental interaction of X-rays with bound electrons can be due to the electron charge or the coupling between the electric and magnetic field of the incident photons with the atomic magnetic moment. Charge scattering is the dominant mechanism and the basis for crystallographic investigation of condensed matter. When we consider the coherent X-ray elastic diffraction on single crystals, the individual atomic scattering amplitudes interfere at different lattice sites n and the elastic scattering cross-section can be written as:

$$\frac{\mathrm{d}\sigma}{\mathrm{d}\Omega} = r_0^2 \left| \sum_n \mathrm{e}^{\mathrm{i}\mathbf{Q}\cdot\mathbf{R}_n} f_n(\mathbf{k}, \mathbf{k}', \hat{\epsilon}, \hat{\epsilon}', \hbar\omega_k) \right|^2 \tag{2}$$

where $f_n(\mathbf{k}, \mathbf{k}', \hat{\epsilon}, \hat{\epsilon}', \hbar\omega_k)$ is the scattering amplitude of the electrons at site n, $\mathbf{R}_n$ is the position of the nth site in the crystal, $\mathbf{Q} = \mathbf{k} - \mathbf{k}'$ is the scattering vector and $r_0 = e^2/mc^2 \approx 2.82 \times 10^{-5}$ Å is the classical electron radius.

The X-ray magnetic scattering gives rise to two regimes, determined by the incident photon energy: the non-resonant limit, which contains the energy independent part of the scattering amplitude and includes the Thomson scattering amplitude $f_0 \propto Zr_0$ and the magnetic scattering amplitude $f^{\mathrm{magn.}}$, and the RXS regime which contains the real f' and imaginary $\mathrm{i}f''$ part of the energy-dependent terms:

$$f = f_0 + f^{\mathrm{magn.}} + f' + \mathrm{i}f'' \tag{3}$$

The resonant terms, also called anomalous or dispersive terms, appear when the incident X-ray energy lies near an absorption edge (i.e. $K, L, M, \ldots$ absorption edges) as a consequence of the photo-absorption effect, and correspond to transitions of core electrons into available electronic states above the Fermi level. For the forward direction the imaginary part of scattering amplitude $f''(\mathbf{Q} = \mathbf{0})$ is related to the absorption cross section:

$$\sigma = \frac{4\pi}{|\mathbf{k}|} \mathrm{Im}\left[\hat{\boldsymbol{\epsilon}}^* \cdot f(\mathbf{Q} = 0)\right] \tag{4}$$

where $\mathbf{Q}$ is the scattering vector and $\mathbf{k}$, $\hat{\boldsymbol{\epsilon}}$ are the wave vector and the polarization of the incident photon beam, respectively.

Photons are defined by the initial state $|\mathbf{k}, \hat{\epsilon}\rangle$ characterized by wavevector $\mathbf{k}$, polarization $\hat{\epsilon}$ and energy $\hbar\omega$. Initially the electrons are found in the state $|a\rangle$, an eigenstate of $\mathcal{H}_{\mathrm{el}}$ with energy E_a. The interaction between electrons and photons creates a new final eigenstate $|b\rangle$ for the electrons with an energy E_b and a scattered photon in the state $|\mathbf{k}', \hat{\epsilon}'\rangle$ with an energy $\hbar\omega'$. The probability of such a transition is given by the Fermi's Golden Rule, which is used in a second order perturbation treatment:

$$W = \frac{2\pi}{\hbar} \left| \langle f|\mathcal{H}'|i\rangle + \sum_n \frac{\langle f|\mathcal{H}'|n\rangle\langle n|\mathcal{H}'|i\rangle}{E_i - E_f} \right|^2 \delta(E_i - E_f) \tag{5}$$

where $|i\rangle = |a; \mathbf{k}, \hat{\epsilon}\rangle$, $|f\rangle = |b; \mathbf{k}', \hat{\epsilon}'\rangle$, $E_i = E_a + \hbar\omega_k$ and $E_f = E_b + \hbar\omega'_k$. For $E_a \neq E_b$ we obtain inelastic scattering and for $E_a = E_b$ we obtain the elastic case. In the following we only consider elastic scattering.

The differential scattering cross-section is defined as:

$$\frac{\mathrm{d}^2\sigma}{\mathrm{d}\Omega\,\mathrm{d}E} = W \cdot \frac{\rho(E_f)}{I_0} \tag{6}$$

with $\rho(E_f)$ being the density of final states accessible to the photon and I_0 the incident photon flux, namely:

$$\rho(E_f) = \frac{V}{(2\pi)^3}\frac{\omega_{k'}^2}{\hbar c^3} \quad \text{and} \quad I_0 = \frac{c}{V} \tag{7}$$

where V is a quantization volume.

Following the perturbative method developed by Blume [23], which considers an unperturbed system described by the electron and non-interacting photon Hamiltonians, the total scattering amplitude for coherent elastic scattering of X-rays can be calculated on the basis of the interaction Hamiltonian $\mathcal{H}'$:

$$\begin{aligned}\mathcal{H}' &= \mathcal{H}'_1 + \mathcal{H}'_2 + \mathcal{H}'_3 + \mathcal{H}'_4 \\ &= \frac{e^2}{2mc^2}\sum_j \mathbf{A}^2(\mathbf{r}_j) - \frac{e}{mc}\sum_j \mathbf{A}(\mathbf{r}_j)\cdot\mathbf{P}_j - \frac{e\hbar}{mc}\sum_j \mathbf{s}_j\cdot\left[\nabla\times\mathbf{A}(\mathbf{r}_j)\right] \\ &\quad - \frac{e\hbar}{2(mc)^2}\frac{e}{c^2}\sum_j \mathbf{s}_j\cdot\left[\dot{\mathbf{A}}(\mathbf{r}_j)\times\mathbf{A}(\mathbf{r}_j)\right]\end{aligned} \tag{8}$$

where m, $\mathbf{P}_j$ and $\mathbf{s}_j$ denote the electron mass, the momentum and the spin operators, respectively, and $\mathbf{A}(\mathbf{r}_j)$ is the vector potential which characterizes the radiation field. We are now in position to calculate, using Fermi's Golden rule Eq. (5), the transition probabilities for the different terms $\mathcal{H}'_i$ associated to the interacting Hamiltonian $\mathcal{H}'$. Because we are interested only in the elastic scattering process which leaves the solid in the same state as before the interaction (scattering processes which conserve the number of photons), we will select the term which contains only both the creation and annihilation of a photon and we neglect the others. The vector potential $\mathbf{A}(\mathbf{r})$ is linear in photon creation and annihilation, so that the conservation of number of photons occurs for even degrees of $\mathbf{A}$.

Therefore, in first order perturbation, only the terms which are quadratic in $\mathbf{A}$ ($\mathcal{H}'_1$ and $\mathcal{H}'_4$), are kept. The linear terms in $\mathbf{A}$ ($\mathcal{H}'_2$ and $\mathcal{H}'_3$) contribute to second order in the perturbation. The Fermi's Golden Rule can written as:

$$W = \frac{2\pi}{\hbar}\left|\langle a;\mathbf{k}'\hat{\epsilon}'|H'_1 + H'_4|a;\mathbf{k}\hat{\epsilon}\rangle + \sum_n \frac{\langle a;\mathbf{k}'\hat{\epsilon}'|H'_2 + H'_3|n\rangle\langle n|H'_2 + H'_3|a;\mathbf{k}\hat{\epsilon}\rangle}{E_a + \hbar\omega_k - E_n}\right|^2 \tag{9}$$

In order to evaluate the coherent elastic scattering cross-section, the scattering amplitudes $f_n(\mathbf{k},\mathbf{k}',\hat{\epsilon},\hat{\epsilon}',\hbar\omega_k)$ can be developed in resonant and non-resonant scattering amplitudes, by assuming that the unperturbed radiation is monochromatic, and the vector potential which characterizes the radiation field is a linearly polarized plane wave. After some manipulations (see Ref. [23]) we can write:

$$\begin{aligned}f_n(\mathbf{k},\mathbf{k}',\hat{\epsilon},\hat{\epsilon}',\hbar\omega) &= \langle a|\sum_j \mathrm{e}^{\mathrm{i}\mathbf{Q}\cdot\mathbf{r}_j}|a\rangle\hat{\epsilon}'\cdot\hat{\epsilon} - \mathrm{i}\frac{\hbar\omega}{mc^2}\langle a|\sum_j \mathrm{e}^{\mathrm{i}\mathbf{Q}\cdot\mathbf{r}_j}\left[\frac{\mathbf{iQ}\times\mathbf{P}_j}{\hbar k^2}\cdot\mathbf{A}' + \mathbf{s}_j\cdot\mathbf{B}'\right]|a\rangle \\ &\quad + \frac{1}{m}\sum_c \frac{E_a - E_c}{\hbar\omega_k}\left(-\frac{\langle a|O^+(\mathbf{k}')|c\rangle\langle c|O(\mathbf{k})|a\rangle}{E_a - E_c + \hbar\omega_k - \mathrm{i}\Gamma_c/2} + \frac{\langle a|O(\mathbf{k})|c\rangle\langle c|O^+(\mathbf{k}')|a\rangle}{E_a - E_c - \hbar\omega_k}\right)\end{aligned} \tag{10}$$

where the first term is the Thomson contribution f_0, the second term the non-resonant X-ray magnetic scattering amplitude $f^{\text{magn.}}$, which will be made explicit in Section 3.2, and the third and fourth terms are the so-called anomalous or resonant contribution $f^{\text{RXS}} = f' + \mathrm{i}f''$. When the incoming photon energy $\hbar\omega$ is very different from any characteristic energy $E_c - E_a$ of the system, we are in the non-resonant regime. If, however, the photon energy is tuned to such a characteristic energy, we are in the resonant regime, where the resonant denominator $\frac{1}{E_a - E_c + \hbar\omega_k - \mathrm{i}\Gamma_c/2}$ of Eq. (10) plays the important role, giving rise to the typical enhancement of the magnetic intensities across the absorption edge. The resonant process consists in promoting an electron from core levels into a valence shell (either partially occupied or empty), and the subsequent decay into the same initial state result in an elastically re-emitted photon, were Γ_c is the width of the excited level $|c\rangle$ with energy E_c and $2\pi\hbar/\Gamma_c$ its life time. The operator $O(\mathbf{k})$ will be analysed in detail in Section 3.3.

3.1. Thomson scattering and polarized photons

The first term of Eq. (10) describes the charge scattering, known as Thomson scattering. It is directly related to the Fourier transform of the charge density:

$$f_0(\mathbf{Q}, \hat{\epsilon}, \hat{\epsilon}') = \langle a| \sum_j \mathrm{e}^{\mathrm{i}\mathbf{Q}\cdot\mathbf{r}_j} |a\rangle \; \hat{\epsilon}' \cdot \hat{\epsilon} \tag{11}$$

To describe the polarization of incident $\hat{\epsilon}$ and scattered $\hat{\epsilon}'$ beams various orthogonal polarization basis vectors can be used. In diffraction experiments two characteristic directions are used to describe the linear polarization of the radiation: the σ polarization perpendicular to the scattering plane and the π polarization lying in the plane.

Using the basis vectors shown in Fig. 2, a generic incident polarisation state can be written as $\vec{\epsilon} = \sigma\hat{\epsilon}_\sigma + \pi\hat{\epsilon}_\pi$, whereas the polarisation of the diffracted beam is $\vec{\epsilon}' = \sigma'\hat{\epsilon}'_\sigma + \pi\hat{\epsilon}'_\pi$. The scalar product between these two vectors, determining the polarization dependence of the diffracted intensity, can then be written as:

$$\vec{\epsilon}' \cdot \vec{\epsilon} = (\sigma'\pi) \begin{pmatrix} 1 & 0 \\ 0 & \cos(2\theta) \end{pmatrix} \begin{pmatrix} \sigma \\ \pi \end{pmatrix} \tag{12}$$

where θ is the scattering angle. The polarization factor tells us that, if the incident radiation is purely polarized along one of the basis vectors, then the charge scattering doesn't change its polarization. This effect is used to select by a single crystal polarization analyzer the linear polarization of the scattered photons, as represented in Fig. 2. A single crystal analyzer is selected and oriented with a scattering angle of $\theta_{an} \approx 45°$ and can be rotated about the scattering vector $\mathbf{k}'$ (angle η). In this specific case (or close to it), we have:

$$\vec{\epsilon}'' \cdot \vec{\epsilon}' = (\sigma''\pi'') \begin{pmatrix} 1 & 0 \\ 0 & \approx 0 \end{pmatrix} \begin{pmatrix} \sigma' \\ \pi' \end{pmatrix} \tag{13}$$

where $\vec{\epsilon}''$ is the photon polarization after diffraction from analyzer crystal.

We can easily see that, in the case of Thomson scattering, when the incident polarization is σ, the scattered intensity is only detected when $\eta = 0°$. The polarization analysis, combined with the rotation ψ of the sample about the scattering vector $\mathbf{Q} = \mathbf{k}' - \mathbf{k}$ (the so-called azimuthal rotation), are the basic method to separate the magnetic or RXS intensities from the charge scattering.

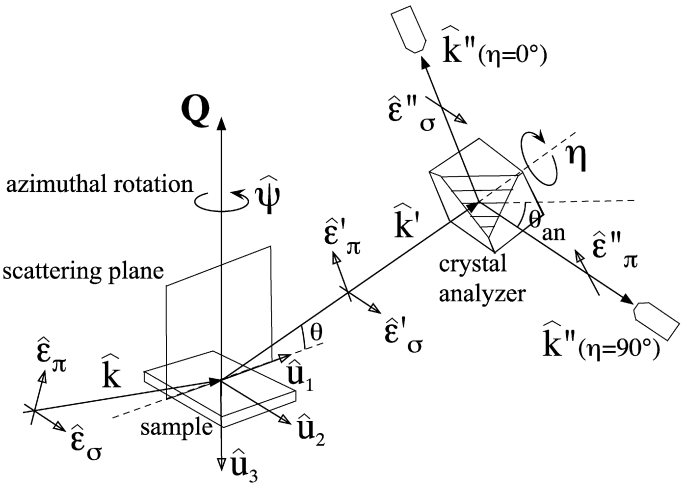

Fig. 2. Description of the vertical scattering geometry with the polarization analysis setup. A crystal analyzer is selected and oriented for a given energy with a Bragg scattering angle $\theta_{\mathrm{an}} \approx 45°$, and it can be rotated about the scattered wavevector $\mathbf{k}'$ (angle η). For scattered photons with polarization $\hat{\epsilon}'_\sigma$ ($\hat{\epsilon}'_\pi$), the intensity is detected when $\eta = 0°$ ($\eta = 90°$).

Fig. 2. Description de la géométrie en diffraction verticale, avec le dispositif d'analyse de polarisation. Pour une énergie donnée, un cristal analyseur est choisi et orienté avec un angle de Bragg $\theta \approx 45°$. Il peut tourner (angle η) autour du vecteur d'onde diffracté $\mathbf{k}'$. Pour les photons diffractés dans la polarisation $\hat{\epsilon}'_\sigma$ ($\hat{\epsilon}'_\pi$), l'intensité est détectée à $\eta = 0°$ ($\eta = 90°$).

3.2. Non-resonant X-ray magnetic scattering

Far from the characteristic energy ($\hbar\omega_k \gg E_c - E_a$) the non-resonant terms f_0 and $f^{\text{magn.}}$ in Eq. (10) are dominant. We can write $f^{\text{magn.}}$ in term of the Fourier transform of the orbital and spin magnetization density $\mathbf{S}(\mathbf{Q})$ and $\mathbf{L}(\mathbf{Q})$, respectively:

$$\mathbf{S}(\mathbf{Q}) = \langle a| \sum_j \mathbf{s}_j e^{i\mathbf{Q}\cdot\mathbf{r}_j} |a\rangle \tag{14}$$

$$\mathbf{L}(\mathbf{Q}) = \langle a| \sum_j \mathbf{l}_j e^{i\mathbf{Q}\cdot\mathbf{r}_j} |a\rangle \tag{15}$$

Then the $f^{\text{magn.}}$ amplitude is given by:

$$\begin{aligned} f^{\text{magn.}} &= -i\frac{\hbar\omega}{mc^2}\left(\frac{1}{2}\mathbf{L}(\mathbf{Q})\cdot\mathbf{A}'' + \mathbf{S}(\mathbf{Q})\cdot\mathbf{B}'\right) \\ &= -i\frac{\hbar\omega}{mc^2}\begin{pmatrix} M_{\sigma\sigma} & M_{\pi\sigma} \\ M_{\sigma\pi} & M_{\pi\pi} \end{pmatrix} \end{aligned} \tag{16}$$

where $\mathbf{A}''$ and $\mathbf{B}'$ are vectors which describe the polarization and wavevector dependence of the magnetic scattering process and the magnetic scattering amplitudes $M_{i,j}$ are decomposed in the basis of vectors $\hat{u}_i$ represented in Fig. 2 as follows:

$$M_{\sigma\sigma} = S_2 \sin 2\theta \tag{17}$$

$$M_{\pi\sigma} = -2\sin^2\theta\big[(\cos\theta)(L_1 + S_1) - S_3\sin\theta\big] \tag{18}$$

$$M_{\sigma\pi} = 2\sin^2\theta\big[\cos\theta(L_1 + S_1) + S_3\sin\theta\big] \tag{19}$$

$$M_{\pi\pi} = \sin 2\theta[2L_2\sin^2\theta + S_2] \tag{20}$$

Here S_i and L_i are the components of $\mathbf{S}(\mathbf{Q})$ and $\mathbf{L}(\mathbf{Q})$ are defined in the coordinate system of $\hat{u}_i$. It can be seen that by taking advantage of the different geometrical prefactors for spin and orbital moments, X-ray magnetic scattering provides the possibility to separate spin and orbital moment contributions to the total magnetization density. In particular, there is no contribution of L to the σ–σ polarization channel. More generally, the prefactors can be adjusted by changing either the scattering geometry or the X-ray polarization. The separation of L and S presents a distinct difference to neutron scattering, where only the total magnetic moment is probed. Moreover, the L/S ratio can be probed in the ordered state, like in antiferromagnetic systems or in modulated structures.

In the case of localized electron systems, L_i and S_i can easily be related to the spin μ_s and orbital μ_l magnetic moments of the i-atom:

$$S_i = \frac{f_s(Q)\mu_s^i}{g_s\mu_B} \tag{21}$$

$$L_i = \frac{f_l(Q)\mu_l^i}{g_l\mu_B} \tag{22}$$

with g_l and g_s being the appropriate Landé factors and μ_B the Bohr magneton. In the spherical dipole approximation the spin and orbital form factors f_l and f_s are usually expressed as:

$$f_s(Q) = \big\langle j_0(Q)\big\rangle \tag{23}$$

$$f_l(Q) = \big\langle j_0(Q)\big\rangle + \big\langle j_2(Q)\big\rangle \tag{24}$$

where $\langle j_i(Q)\rangle$ are radial integrals used in the theoretical development of the magnetic form factors. The orbital magnetic moment, created by the orbital currents, is more localized than the spin magnetization, therefore its form factor falls down less rapidly in reciprocal space.

The method of separation of L/S has been applied successfully on simple transition metal oxides [24,25], in actinides [26], Jahn–Teller cuprates [27], strongly correlated electron systems [17].

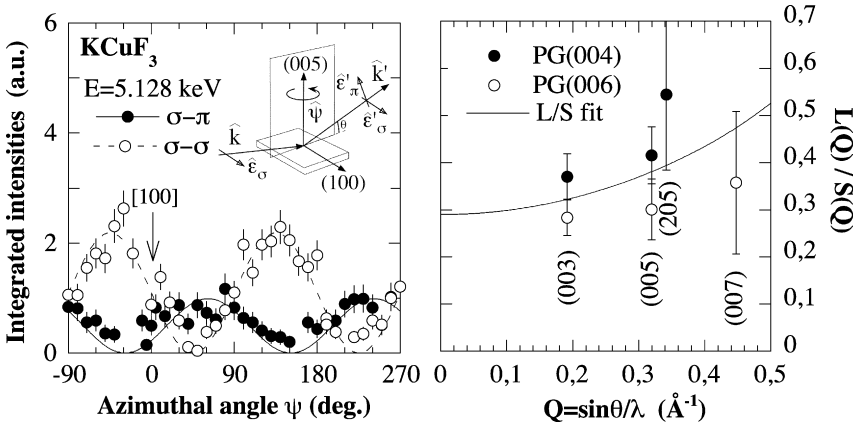

Fig. 3. Left: Azimuthal dependence of antiferromagnetic reflection (005) taken at 11 K in non-resonant regime ($E = 5.128$ keV). The maximum of σ–σ' intensity corresponds to the moment direction μ pointing along the $\langle 110 \rangle$ direction. Right: L/S ratio in $KCuF_3$ as a function of scattering vector Q [27].

Fig. 3. A gauche : dépendance azimutale de la réflexion antiferromagnétique (005) mesurée à 11 K dans le régime non résonnant ($E = 5{,}465$ keV). Le maximum de l'intensité σ–σ' correspond à la direction des moments μ pointant le long de $\langle 110 \rangle$. A droite : le rapport L/S dans $KCuF_3$ en fonction du vecteur de diffusion Q [27].

For example, the Mott–Hubbard $KCuF_3$ insulator is one of those rare examples where one-dimensional magnetic properties are manifested within a pseudo-cubic crystal structure. The magnetic structure was determined by neutron elastic scattering measurements, and corresponds to the type-I antiferromagnetic below $T_N = 38$ K, with the magnetic moment direction perpendicular to the cubic c-axis [28]. Far from the absorption edge, a forbidden lattice reflection appears below the Néel temperature with a propagation vector $\mathbf{q}_m = (001)$. Magnetic reflections like (001), (003) (005) can be reached by orienting the crystal along the axis $\langle 00l \rangle$. In this experiment the vertical scattering geometry was used. The azimuthal scans show well defined maxima and minima (Fig. 3-left), which prove that a single magnetic domain was probed. For this particular geometry, and by analyzing the sinusoidal dependence of scattered signal, it is easy to determine the magnetic moment directions in the plane, directed along the $\langle 110 \rangle$ direction of the pseudo-cubic perovskite cell.

Because the Cu magnetic moments lie in the basal plane ($S_3 = 0$), in this case only two non-resonant X-ray scattering amplitudes associated to the channel σ–σ' and σ–π' can be considered:

$$M_{\sigma\sigma} = S_2 \sin 2\theta \tag{25}$$

$$M_{\pi\sigma} = -2\sin^2\theta\big[(\cos\theta)(L_1 + S_1)\big] \tag{26}$$

The ratio of orbital $L(Q)$ and spin $S(Q)$ moments are thus given by the simplified expression:

$$\frac{L(Q)}{S(Q)} = \frac{\tan(\rho - \frac{\pi}{4})}{\sin\theta}\sqrt{\frac{I_{\sigma\pi}}{I_{\sigma\sigma}}} - 1 \tag{27}$$

where ρ is defined as the angle between the [100] direction and the $\hat{\mathbf{u}}_1$ direction. By measuring the intensity ratios between different magnetic reflections, it is possible calculate the values L/S as a function of scattering wavevector Q, as shown in Fig. 3-right. The extrapolation to $Q = 0$ suggest a ratio of $\langle L \rangle / 2\langle S \rangle = 0.14 \pm 0.08$ between orbital angular momentum and spin contributions to the magnetic moment [27].

The non-resonant X-ray scattering regime has also important applications in the domain of spin-density waves [29], charge density waves [30] or surface magnetism that exploits surface refraction effects of the charge scattering, in order to disentangle the magnetic and structural contributions from magnetic surfaces [31].

3.3. Resonant X-ray scattering

The RXS amplitude f^{RXS} associated to the third term of Eq. (10) depends on the intermediate states $|c\rangle$ of the atomic system and has a specific dependence on the incident photon energy $\hbar\omega_k$. Each numerator of the anomalous

term contains a dependence on the features of an intermediate state $|c\rangle$ (an eigenstate of the unperturbed solid). This dependence is enclosed in two matrix elements of the interaction Hamiltonian, in such a way that this physical phenomenon can be viewed as a *virtual transition* of the matter, initially lying in the $|a\rangle$ state, *to* and *from* the $|c\rangle$ state. This experience involves the promotion of a core electron to a higher unoccupied level, and its decay to the original core level. Conversely, during this process, the photon is first absorbed, then re-emitted with a different direction and polarization. The sensitivity to magnetic moments comes from the Pauli's principle and the spin–orbit interaction. The Pauli's principle ensures the availability of the intermediate states near the resonance energy. The spin–orbit interaction play a role both in the core levels with non-vanishing orbital moment $l \neq 0$, as in the case of L_2- and L_3-edges of rare earths, or in the much weaker spin–orbit interaction of valence states, as in the case of K-edge of transition metals, where the s core levels have no spin–orbit interaction. The consequence is that the anomalous scattering is an important tool to investigate not only the local site anisotropy of an atom within a crystalline structure, but it is also sensitive to the degeneracy of electronic states with specific orbital character. In fact, the atomic scattering amplitude can vary substantially depending on the occupation of selected spin and orbital states, and therefore on their availability to serve as intermediate states in the second order scattering process.

Starting from the third term in Eq. (10) containing the resonant contribution, we can express the resonant scattering amplitude as:

$$
\begin{aligned}
f^{\mathrm{RXS}} = -\frac{1}{m}\sum_c \frac{E_a - E_c}{\hbar\omega_k}\cdot\Bigg[\hbar^2 \frac{\langle a|\sum_j \mathrm{e}^{-\mathrm{i}\mathbf{k}'\cdot\mathbf{r}_j}(\mathbf{k}'\times\epsilon')\cdot\mathbf{s}_j|c\rangle\langle c|\sum_j \mathrm{e}^{\mathrm{i}\mathbf{k}\cdot\mathbf{r}_j}(\mathbf{k}\times\epsilon)\cdot\mathbf{s}_j|a\rangle}{E_a - E_c + \hbar\omega_k - \mathrm{i}\Gamma_c/2} \\
+ \hbar\Bigg(\frac{\langle a|\sum_j \mathrm{e}^{-\mathrm{i}\mathbf{k}'\cdot\mathbf{r}_j}\epsilon'\cdot\mathbf{P}_j|c\rangle\langle c|\sum_j \mathrm{e}^{\mathrm{i}\mathbf{k}\cdot\mathbf{r}_j}(\mathbf{k}\times\epsilon)\cdot\mathbf{s}_j|a\rangle}{E_a - E_c + \hbar\omega_k - \mathrm{i}\Gamma_c/2} \\
- \frac{\langle a|\sum_j \mathrm{e}^{-\mathrm{i}\mathbf{k}'\cdot\mathbf{r}_j}(\mathbf{k}'\times\epsilon')\cdot\mathbf{s}_j|c\rangle\langle c|\sum_j \mathrm{e}^{\mathrm{i}\mathbf{k}\cdot\mathbf{r}_j}\epsilon\cdot\mathbf{P}_j|a\rangle}{E_a - E_c + \hbar\omega_k - \mathrm{i}\Gamma_c/2}\Bigg) \\
+ \frac{\langle a|\sum_j \mathrm{e}^{-\mathrm{i}\mathbf{k}'\cdot\mathbf{r}_j}\epsilon'\cdot\mathbf{P}_j|c\rangle\langle c|\sum_j \mathrm{e}^{\mathrm{i}\mathbf{k}\cdot\mathbf{r}_j}\epsilon\cdot\mathbf{P}_j|a\rangle}{E_a - E_c + \hbar\omega_k - \mathrm{i}\Gamma_c/2}\Bigg]
\end{aligned}
\tag{28}
$$

The first term depends only on the spin. It is proportional to S^2 and therefore does not give rise to a pure antiferromagnetic Bragg peak, but it contributes however to anomalous scattering. The second term, which has been used by Namikawa et al. [14] to describe resonant phenomena in ferromagnetic nickel, is smaller, by a factor of $\hbar\omega/mc^2$ compared to last term and can be neglected. In addition this term vanishes at $\mathbf{Q} = 0$ and thus cannot induce a magnetic circular dichroism signal.

Usually in resonant X-ray magnetic scattering only the last term is taken into account to discuss the magnetic resonant scattering amplitudes. Its physical nature arises from the scalar product $\mathbf{A}\cdot\mathbf{P}_j$ in the original Hamiltonian (Eq. (8)):

$$
f^{\mathrm{RXS}} = -\frac{1}{m}\sum_c \frac{E_a - E_c}{\hbar\omega_k}\cdot\frac{\langle a|\sum_j \mathrm{e}^{-\mathrm{i}\mathbf{k}'\cdot\mathbf{r}_j}\epsilon'\cdot\mathbf{P}_j|c\rangle\langle c|\sum_j \mathrm{e}^{\mathrm{i}\mathbf{k}\cdot\mathbf{r}_j}\epsilon\cdot\mathbf{P}_j|a\rangle}{E_a - E_c + \hbar\omega_k - \mathrm{i}\Gamma_c/2} \tag{29}
$$

Eq. (29) was developed by Hannon et al. [15] in term of dipole approximation, i.e. by developing $\mathrm{e}^{\mathrm{i}\mathbf{k}\cdot\mathbf{r}_j} \approx 1 + \mathrm{i}\mathbf{k}\cdot\mathbf{r}_j - (\mathbf{k}\cdot\mathbf{r}_j)^2/2 + \cdots$ as a power series and retaining only the two first dominant contributions.

Note that the usual *optical approximation*, based on the fact that $\mathbf{k}\cdot\mathbf{r}_j \ll 1$, cannot be assumed in this case. In fact, at X-ray frequencies, the wave vector is of the same order of magnitude than the atomic sizes. The Hannon's term in Eq. (29) can be rewritten in four distinct terms by using the previous relations and the dipole $\sum_j \mathbf{r}_j$ and the quadrupole $\sum_j \frac{\mathrm{i}}{2}\mathbf{r}_j(\mathbf{k}'\cdot\mathbf{r}_j)$ operators:

$$
\begin{aligned}
f^{\mathrm{RXS}} \approx m \sum_c & \frac{(E_c - E_a)^3}{\hbar^3 \omega_k \, (E_a - E_c + \hbar\omega_k - \mathrm{i}\Gamma_c/2)} \\
& \times \left[\hat{\epsilon}' \cdot \langle a| \sum_j \mathbf{r}_j |c\rangle\langle c| \sum_i \mathbf{r}_i |a\rangle \cdot \hat{\epsilon} - \mathrm{i}\hat{\epsilon}' \cdot \langle a| \sum_j \frac{1}{2}\mathbf{r}_j(\mathbf{k}' \cdot \mathbf{r}_j)|c\rangle\langle c| \sum_i \mathbf{r}_i |a\rangle \cdot \hat{\epsilon} \right. \\
& \left. + \mathrm{i}\hat{\epsilon}' \cdot \langle a| \sum_j \mathbf{r}_j |c\rangle\langle c| \sum_i \frac{1}{2}\mathbf{r}_i(\mathbf{k} \cdot \mathbf{r}_i)|a\rangle \cdot \hat{\epsilon} + \hat{\epsilon}' \cdot \langle a| \sum_j \frac{1}{2}\mathbf{r}_j(\mathbf{k}' \cdot \mathbf{r}_j)|c\rangle\langle c| \sum_i \frac{1}{2}\mathbf{r}_i(\mathbf{k} \cdot \mathbf{r}_i)|a\rangle \cdot \hat{\epsilon} \right] \\
= {} & f^{\mathrm{RXS}}(dd) + f^{\mathrm{RXS}}(dq) + f^{\mathrm{RXS}}(qq)
\end{aligned} \tag{30}
$$

where the different contribution are thus classified in the following way:

- $f^{\mathrm{RXS}}(dd)$: (E1–E1) dipole–dipole;
- $f^{\mathrm{RXS}}(dq)$: (E1–E2) dipole–quadrupole;
- $f^{\mathrm{RXS}}(qq)$: (E2–E2) quadrupole–quadrupole.

The different terms are composed by factors which show a different set of symmetries under inversion, rotation and time-reversal.

Using the Cartesian reference coordinate system defined in Eq. (13) for the photon polarization, we can develop the scalar product of Eq. (30). The scattering amplitude for RXS can be written in the form:

$$
\begin{aligned}
f^{\mathrm{RXS}} \approx m \sum_c & \frac{(E_c - E_a)^3}{\hbar^3 \omega_k \, (E_a - E_c + \hbar\omega_k - \mathrm{i}\Gamma_c/2)} \\
& \times \left[\sum_{\alpha\beta} \epsilon'^*_\alpha \, \epsilon_\beta \, D^{\alpha\beta} - \frac{\mathrm{i}}{2} \sum_{\alpha\beta\gamma} \epsilon'^*_\alpha \, \epsilon_\beta (k_\gamma I^{\alpha\beta\gamma} - k'_\gamma I^{*\beta\alpha\gamma}) + \frac{1}{4} \sum_{\alpha\beta\gamma\delta} \epsilon'^*_\alpha \epsilon_\beta k'_\gamma k_\delta Q^{\alpha\beta\gamma\delta} \right]
\end{aligned} \tag{31}
$$

where α, β, γ, δ are indexes which vary independently over the three Cartesian directions x, y, z, and we have used the following shorthand notation for the transition matrix elements:

$$D^{\alpha\beta} = \langle a| \sum_j r_j^\alpha |c\rangle\langle c| \sum_i r_i^\beta |a\rangle \tag{32}$$

$$I^{\alpha\beta\gamma} = \langle a| \sum_j r_j^\alpha |c\rangle\langle c| \sum_i r_i^\beta r_i^\gamma |a\rangle \tag{33}$$

$$Q^{\alpha\beta\gamma\delta} = \langle a| \sum_j r_j^\alpha r_j^\beta |c\rangle\langle c| \sum_i r_i^\gamma r_i^\delta |a\rangle \tag{34}$$

where the transition matrix elements $D^{\alpha\beta}$, $I^{\alpha\beta\gamma}$ and $Q^{\alpha\beta\gamma\delta}$ associated to E1–E1, E1–E2 and E2–E2 contributions of Eq. (31) turn out to be characterized by Cartesian tensors of second, third and fourth rank, respectively [18].

3.4. Symmetries

It is important to determine the invariant behavior of the tensors D, I and Q under the following symmetry transformations of the coordinate system:

- Space inversion or parity;
- Rotation;
- Time-reversal.

In fact, the magnetic atoms in the unit cell are related by symmetry operations and the site symmetry of the individual atoms has important implications for the possible allowed resonant transitions defined by the matrix elements of Eq. (34).

3.4.1. Space inversion

Both tensors D and Q are even under the inversion symmetry. In fact, they can be expressed as a product of two matrix elements both containing an odd or even number of coordinates r_i. This leads to an even final product. This is not true in the case of the tensor I which is odd under inversion symmetry operation, as it is made up of an odd number of position operators.

As a result, if an atom sits in an inversion center, the I tensor must be zero, or, in other words, dipole–quadrupole transition (E1–E2) are only allowed for atoms breaking the inversion symmetry.

3.4.2. Rotation

Let us recall that in general, when acting with the rotation group on a rank-n Cartesian tensor, we represent the evolution of the 3^n elements of the tensor by a $3^n \times 3^n$ matrix, which transforms them from their initial values to the rotated ones. If the tensor is reducible, by making an appropriate basis change in the tensor space, we can block diagonalize the rotation matrix into smaller subsets (the so-called irreducible components). This operation corresponds to find the bases of all independent subspaces within the tensor space: each projection of the total tensor into a subspace transforms within that space, under the effect of the rotation group. It can be demonstrated, by a study of the rotation group in three spatial dimensions, that every irreducible representation is labeled by an integer value j: for a given j, the dimension of the representation (in the tensor space) is $2j + 1$.

The new n^2 elements, expressed in the irreducible bases, are found as linear combination of the initial ones, and are re-arranged in several sub-groups labeled by j. Within each group, the $2j + 1$ parameters transform under rotation as the $2j + 1$ components of the spherical harmonic function $Y_j^m(\theta, \phi)$, where m assumes the values $-j, \ldots, j$. It means they are examples of spherical tensors of rank j.

In conclusion, if we decompose each tensor element $D^{\alpha\beta}$ (or $I^{\alpha\beta\gamma}$, or $Q^{\alpha\beta\gamma\delta}$) into its irreducible components, and substitute it in Eq. (31), then we have a picture of the behavior of the atomic part of the scattering amplitude under rotation, i.e. about its rotational symmetries.

For example, in the case of E1–E1 term the decomposition of a rank-two tensor (9 parameters) leads to three irreducible representation of rank $j = 0$ (1 parameter), 1 (3 parameters), 2 (5 parameters), in order to have $9 = 1 + 3 + 5$. The decomposition is unique, given a reference axis z:

$$j = 0: \tag{35}$$

$$T_0^{(0)} = \frac{1}{3}(D^{xx} + D^{yy} + D^{zz})$$

$$j = 1: \tag{36}$$

$$T_0^{(1)} = \frac{1}{2}(D^{xy} - D^{yx})$$

$$T_{\pm 1}^{(1)} = \mp\frac{1}{2\sqrt{2}}\left[(D^{yz} - D^{zy}) \mp \mathrm{i}(D^{xz} - D^{zx})\right]$$

$$j = 2: \tag{37}$$

$$T_0^{(2)} = D^{zz} - T_0^{(0)}$$

$$T_{\pm 1}^{(2)} = \mp\sqrt{\frac{2}{3}}\frac{1}{2}\left[(D^{xz} + D^{zx}) \mp \mathrm{i}(D^{yz} + D^{zy})\right]$$

$$T_{\pm 2}^{(2)} = \frac{1}{\sqrt{6}}\left[2D^{xx} - 2D^{yy} \pm \mathrm{i}(D^{xy} + D^{yx})\right]$$

Then, one should re-arrange the result, by coupling together the terms with the same $T_m^{(j)}$; this leads to the following final formula:

$$f^{\mathrm{RXS}}(dd) \propto \sum_{\alpha\beta} \epsilon_\alpha'^* D^{\alpha\beta} = \sum_{j=0,1,2} \sum_{m=-j}^{j} (-1)^{j+m} P_{-m}^{(j)} T_m^{(j)} \tag{38}$$

where $P^{(j)}$ are spherical tensors constructed from the polarization vectors ϵ and ϵ' starting with the Cartesian components $\epsilon_\alpha'^*$ and ϵ_β, and developing it in spherical tensors, just as was done for $D^{\alpha\beta}$.

This result is of importance because, even if we do not have an explicit expression for the scattering amplitude, we can at least recognize that, when the *atom* is rotated with respect to the *radiation field*:

- The $j = 0$ term in the summation is a scalar invariant;
- The three terms $j = 1$ vary as a vector;
- The five terms $j = 2$ vary as a spherical rank two tensor.

The analysis of the other terms E1–E2 and E2–E2 term is carried out in the same way, although the decomposition is no longer unique.

3.4.3. Time-reversal

The time-reversal symmetry exchange the incident and the scattered wavevectors, which corresponds to exchanging the $(\alpha, \beta, \gamma, \delta)$ indexes in Eq. (30). For example, in the case of E1–E1 transitions, the $j = 0$ and $j = 2$ terms involve only symmetric components in the form $D_{+}^{\alpha\beta} = D^{\alpha\beta} + D^{\beta\alpha}$. Conversely, the $j = 1$ term involves only antisymmetric components, which have the form $D_{-}^{\alpha\beta} = D^{\alpha\beta} - D^{\beta\alpha}$. The conclusion is that the $j = 1$ term is the only one which is sensitive to the magnetism of the atom, and identifies to a vector which turns to have all the characteristics of a magnetic moment (axial under inversion, odd under time reversal). The $j = 0$ term does not depend on magnetism and, moreover, shows no anisotropic character: so, it is just charge-sensitive, like the Thomson term. The $j = 2$ term is also independent on magnetism, but its anisotropic behavior suggests a sensitivity to the orientation of the electronic wavefunctions in space and to their symmetries.

The same analysis can be developed for E1–E2 and E2–E2 contributions, and the resonant X-ray scattering amplitude can be expressed in general as a scalar product of two irreducible spherical tensors:

$$f_j^{\mathrm{RXS}} = \sum_{p,q} (-1)^q X_{-q}^{(p)} F_q^{(p)}(j;\omega) \tag{39}$$

where $X_q^{(p)}$ depends only on the incident and scattered polarization and wavevector, while $F_{-q}^{(p)}(j;\omega)$ is associated to the tensorial properties of the j-atom, and can be represented in terms of multipole expansion. The rank p defines the order of multipole in the electromagnetic field expansion and the projection q can take $(2p + 1)$ values that satisfy $(-p \leqslant q \leqslant p)$. $p = even$ tensors are time-even, i.e. invariant under time reversal, whereas $p = odd$ tensor are time-odd [32].

The classification of E1–E2 transitions which involve the operator I has been developed in Refs. [20,18]. The classification of the tensors associated to the multipole expansion are summarized in Table 2 [21].

Table 2
Identification of properties under time-reversal $\hat{T}$ and parity $\hat{P}$ of tensors associated to the multipole expansion

Tableau 2
Propriétés de symétrie dans les inversion de temps $\hat{T}$ et d'espace $\hat{P}$, des tenseurs associés au développement en multipôles

Tensor	rank	$\hat{T}$	$\hat{P}$	Type	Multipole
$F^{(0)}$ (E1–E1)	0	+	+	charge	monopole
$F^{(0)}$ (E2–E2)	0	+	+	charge	monopole
$F^{(1)}$ (E1–E1)	1	−	+	magnetic	dipole
$F^{(1)}$ (E2–E2)	1	−	+	magnetic	dipole
$F^{(1+)}$ (E1–E2)	1	+	−	electric	dipole
$F^{(1-)}$ (E1–E2)	1	−	−	polar toroidal	dipole
$F^{(2)}$ (E1–E1)	2	+	+	electric	quadrupole
$F^{(2)}$ (E2–E2)	2	+	+	electric	quadrupole
$F^{(2+)}$ (E1–E2)	2	+	−	axial toroidal	quadrupole
$F^{(2-)}$ (E1–E2)	2	−	−	magnetic	quadrupole
$F^{(3)}$ (E2–E2)	3	−	+	magnetic	octupole
$F^{(3+)}$ (E1–E2)	3	+	−	electric	octupole
$F^{(3-)}$ (E1–E2)	3	−	−	polar toroidal	octupole
$F^{(4)}$ (E2–E2)	4	+	+	electric	hexadecapole

The physics of multipole ordered states is one of the most exciting research domain of investigation of electronic and magnetic properties of condensed matter. In particular, a possible link between the magnetoelectric effects and toroidal moments in Shubnikov group can be applied to derive a possible origin of superconductivity in electric and magnetic crystals [33].

4. Experiments

The different terms involved in the multipolar expansions E1–E1, E1–E2 and E2–E2 contain tensors of different rank. As a result, the tensorial character of different scattering amplitude in Eq. (2) can lead to a breakdown of the extinction rules valid for the crystal structure, giving rise to a forbidden lattice reflections measurable in Bragg diffraction only when the photon energy corresponds to the characteristic energy of the atomic system under investigation. For example, the case of RXS on V_2O_3 is indicative to describe the complexity of the theoretical interpretation of RXS results but also the potentiality of the RXS methods to study the physics of strongly correlated electron systems. At room temperature vanadium sesquioxide crystallizes in the α-corundum structure as α-Fe_2O_3 (space group $R\bar{3}c$), which can be described with a pseudo-hexagonal space group. The stoichiometric compound V_2O_3 undergoes a strong volume contraction from paramagnetic metal (PM) to antiferromagnetic insulating state (AFI) at $T_N = 150$ K, with a monoclinic (space group I2/a) first order transition. Chromium doping induces a Mott transition into a paramagnetic insulating (PI) state at room temperature, whereas the AFI state arises at $T_N = 180$ K, with a moderate volume contraction [17]. At room temperature (300 K) forbidden lattice reflections $(00{\cdot}l)_H$ with $l = 3(n+1)$ appear at the V K pre-edge, as shown in Fig. 4 for the reflection $(00{\cdot}3)_H$ (defined in the pseudo-hexagonal space group). This feature is common to all the Corundum sesquioxides as α-Fe_2O_3 and Cr_2O_3 [35]. These energy scans show well defined resonances in a narrow energy range of about 2 eV around 5.465 keV, with the azimuthal scans showing the 3-fold symmetry. These amplitudes are associated to the $1s \rightarrow 3d$ (electric quadrupole transition E2), whereas the electric dipole (E1) transitions $1s \rightarrow 4p$ are forbidden for this class of reflections [36]. The analysis of the azimuthal and polarization dependence of these resonances showed that they can be attributed to the parity-even and high order multipoles associated to the electric hexadecapole $F^{(4)}$ (E2–E2) and to the parity-odd electric octupole $F^{(3+)}$ (E1–E2) due to the lack of inversion symmetry at the V-site [37].

In the low-temperature AFI phase, the 3-fold symmetry is lost due to the monoclinic transition and the equivalent forbidden reflection $(10\bar{1})_m$ shows a dominant contribution due to the electric quadrupole $F^{(2+)}$ (E1–E1) in a broad energy region of about 20 eV around 5.475 keV. The $F^{(4)}$ (E2–E2) and $F^{(3+)}$ (E1–E2) contributions are also present in the pre-edge, but they are strongly affected by the interference effect due to the $F^{(2+)}$ (E1–E1) contribution. All these effects are due to the anomalous tensor susceptibility (ATS), called also Templeton scattering, and at the K-edge these class of resonance can be found when local site symmetry breaking is reproduced in a cell by a glide plane or a screw axis. The symmetry breaking can be associated to Jahn–Teller distortions, as in the case of orbital ordering in manganites [38].

In the AFI state, two new classes of reflections appear, with the intensities several order of magnitude lower than the previous one, and associated to the magnetic part of scattering amplitude, i.e. they are time odd. For example, the reflection $(2\bar{2}1)_m$ corresponds to the class defined by the selection rule $k + l = even$ and $h = even$, and corresponds to the magnetic reflections found also by neutron scattering. In fact, the non-resonant magnetic intensity is present far from the absorption edge, as we can see from the low energy part of the spectra. The broad resonance observable in the σ–π' channel only is due to the magnetic dipole $F^{(1)}$ (E1–E1) and associated to the magnetic polarization of the $4p$ V bands, whereas the pre-edge region contains a resonance centered at $E = 5.465$ keV which appears in both the polarization channels. This last resonance contains probably both the time odd magnetic octupole $F^{(3)}$ (E2–E2) and the parity even magnetic quadrupole, but the analysis of the tensorial character of this resonance is complicated by the presence of the strong interference with the dominant magnetic dipole term $F^{(1)}$ (E1–E1). The forbidden lattice reflections with $k + l = even$ and $h = odd$ are visible only when we tune the incident photon energy around the narrow pre-edge, and they are a direct observation of orbital magnetization in the V $3d$ valence shell [17]. This is because of the selection rules, the E1–E1 dipole electric multipoles associated to the virtual transitions toward the $4p$ states are absent, and only high order multipoles contribute to these class of reflections, as in the case of the $(3\bar{3}1)_m$. The azimuthal dependence shows a peculiar polarization behavior on both the polarization channels, and considerations based on the chemical and magnetic space groups, determined previously by neutron diffraction [39], have lead to the conclusion that these resonant reflections are assigned to a parity-odd high order multipoles, specifically to the toroidal

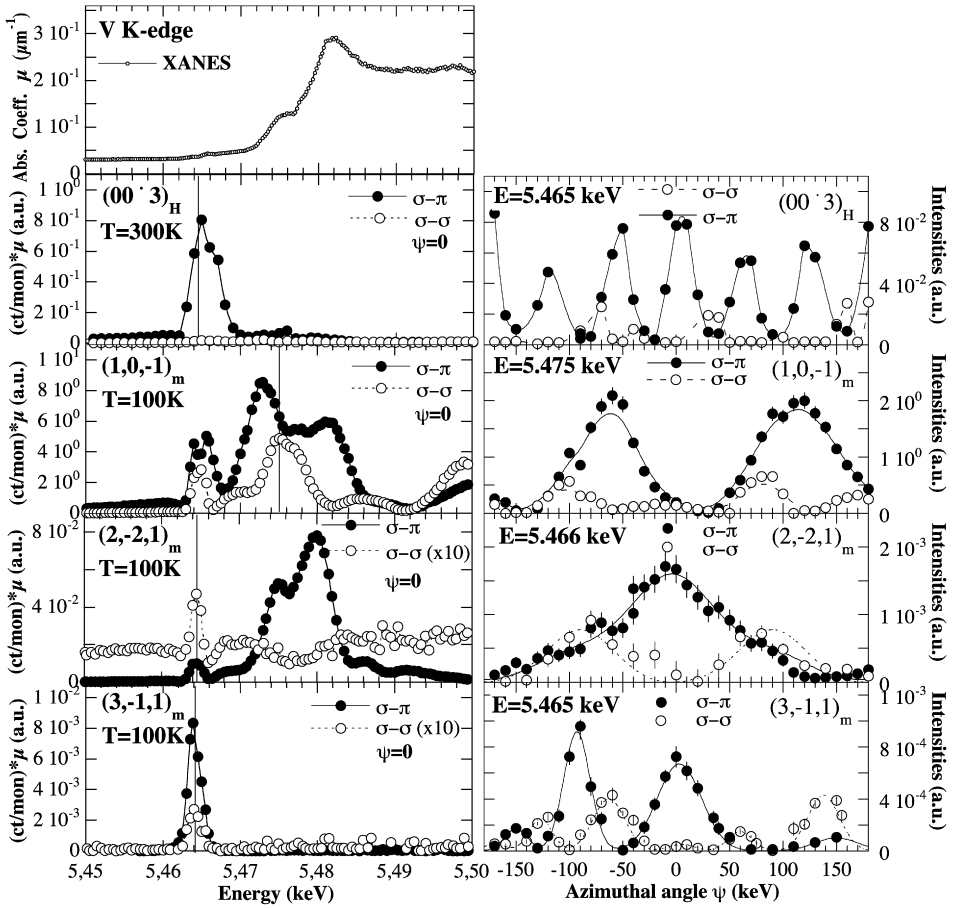

Fig. 4. Energy scans across the V K-edge (left) and the corresponding azimuthal dependence (right) of different classes of forbidden lattice reflections found at room temperature and in the low-temperature antiferromagnetic phase ($T = 100$ K) of 2.8% Cr-doped V_2O_3. Black (white) dots refer to the σ–π' (σ–σ') polarization channel [17,34].

Fig. 4. Dépendances en énergie mesurées au seuil K du Vanadium (à gauche) et en azimuth relatif (à droite) pour différentes classes de réflexions interdites par le groupe d'espace et observées à température ambiente et dans la phase antiferromagnétique à basse température ($T = 100$ K) de V_2O_3 dopé à 2,8 % de Cr. Les points noirs (blancs) représentent le canal de polarisation σ–π' (σ–σ') [17,34].

octupole $F^{(3-)}$ (E1–E2) and to the magnetic octupole $F^{(3)}$ (E2–E2) [18,19]. The observation of these reflections and their interpretation in term of time-reversal and parity breaking symmetries have opened a large debate during the last years, acting as a driving force to improve theories and experiments. The advance of calculations and prediction using ab-initio simulations, based on multiple scattering theory and a relativistic extension of the Schrödinger expansion [40], have opened the avenue to a new class of experiments, in which more degrees of freedom have been introduced to disentangle the high order multipole resonances, as for example the use of phase plate polarimetry to change the incident linear polarization and the full analysis of the Stokes parameters of the scattered light [41].

The chemical selectivity of the RXS cross-sections can be exploited to extract information on the magnetic structure of materials with two sublattice magnetization, as in the case of the non-collinear structure of Co-doped $CeFe_2$, represented in Fig. 5. The Fe sublattice can be studied by exploiting the Fe K-edge and the Ce sublattice by tuning the incident energy at the Ce L_3-edge. In this system the dominant resonant process in both the edges is the magnetic dipole $F^{(1)}$ (E1–E1), and the azimuthal dependence in this case have simple relationship with the incident and scattered polarization, allowing the determination of the sublattice magnetization in the single magnetic domain probed by the experiment [48].

The evolution of the RXS technique with the introduction of an external degree of freedom such as low temperatures, high magnetic field and high pressure open new possibilities of investigation of complex magnetic materials

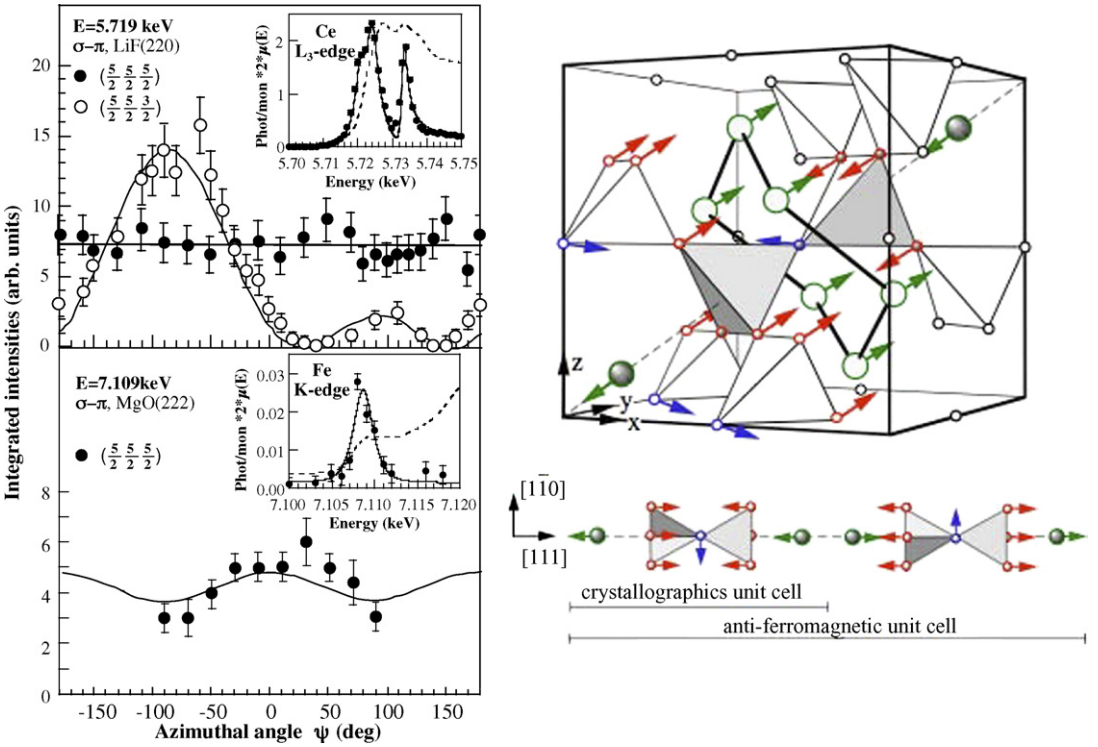

Fig. 5. Left: Azimuthal dependence of the antiferromagnetic reflections in $Ce(Co_{0.07}Fe_{0.93})_2$ taken at Ce L_3-edge (top panel) and Fe K-edge (bottom panel). The inserts show their energy dependence at Ce L-edge (top) and Fe K-edge (bottom). Right: Magnetic structure determined by combining RXS and neutron scattering results, showing the non-collinear Fe sublattice [48].

Fig. 5. A gauche : dépendance azimutale des réflexions antiferromagnétiques mesurées dans $Ce(Co_{0,07}Fe_{0,93})_2$ au seuil Ce L_3 (cadre supérieur) et Fe K (cadre inférieur). Les cadres insérés montrent les dépendances en énergie de ces réflexions aux mêmes seuils. A droite : structure magnétique déterminée en combinant les résultats de diffraction magnétique résonnante des rayons X et de diffraction de neutrons ; on voit le sous-réseau de Fe, non colinéaire [48].

which simultaneously display several types of long-range electronic order. The combination of an external applied magnetic field and RXS gives unique possibilities to investigate the complex relationships between the correlated microscopic properties of magnetic materials. Magnetic fields act directly on the exchange interactions between the magnetic elements and allows fine tuning of the delicate balance between different correlation effects: influence the domain formation (magnetic annealing, single domain studies), induce magnetic phase transitions (metamagnetism, frustrated magnetism in low-dimensional magnets), remove the degeneracy of complex magnetic structures (multi-k magnetic structures). Recently, new families of rare-earth transition metal oxides have been discovered which display a surprisingly large coupling between the ferroelectric and magnetic order parameters, the so-called *multi-ferroics*. This opens up novel possibilities to control magnetism with electric fields, or correspondingly to manipulate ferroelectricity by magnetic fields. Combining the advantages of RXS with the new magnet facility developed on the ID20 beamline [42] allowed the phase diagram of $TbMnO_3$ to be studied in great detail (Fig. 6). For example, for all of the phases identified by the bulk studies we were able to study the underlying chemical and magnetic structures. As a result, the different commensurate (C) and incommensurate (IC) phases can be studied in details, and the contribution to the X-ray diffraction signals from Tb of Mn electrons can be distinguished as well as the corresponding magnetic and electronic modulations within each phase. This allowed us, amongst other things, to establish that the flop of the polarization along the a-axis is driven by an incommensurate to commensurate transition [43].

The application of high pressures at low temperatures on strongly correlated electron systems leads to variations manifested in the electronic structure. By acting on the lattice parameter, hydrostatic pressure may vary the overlap of

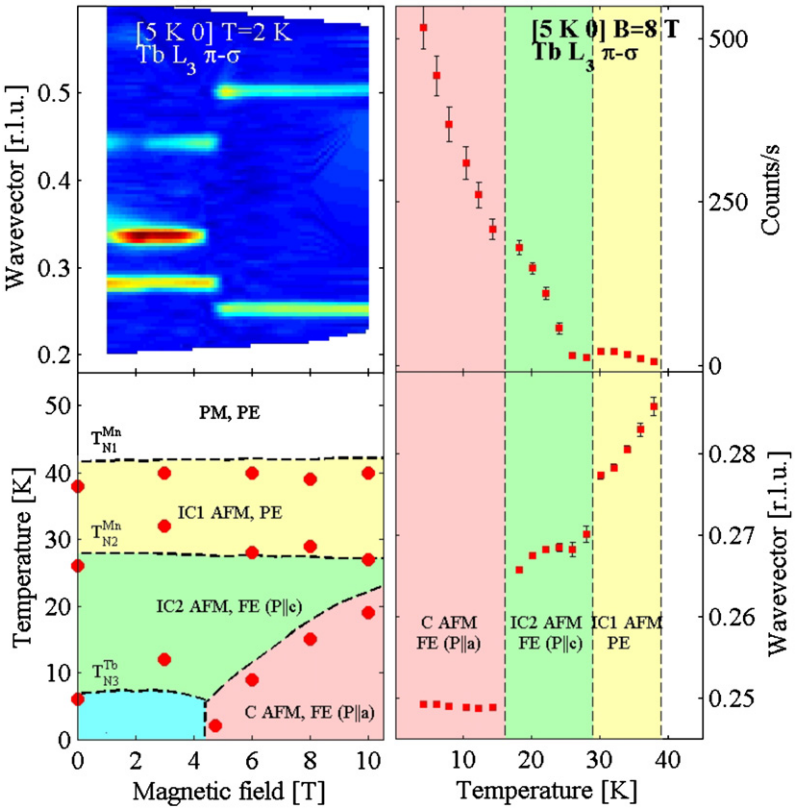

Fig. 6. Left: Magnetic field dependence of RXS at the Tb L_3-edge for (5 k 0) satellite reflections at 2 K (top) and the corresponding H–T phase diagram (bottom). Right: Evolution of the intensity (top) and the wavevector (bottom) of the satellite reflection (5 k 0) as a function of the temperature, under an applied magnetic field of 8 T [43].

Fig. 6. A gauche : dépendance par rapport au champ magnétique, de la diffusion résonnante des rayons X au seuil Tb L_3 pour la réflexion satellite (5 k 0) à 2 K (en haut) et diagramme de phase H–T correspondant (en bas). A droite : évolution de l'intensité (en haut) et du vecteur d'onde (en bas) pour la réflexion satellite (5 k 0) en fonction de la température, sous un champ magnétique appliqué de 8 T [43].

orbitals, thus altering the balance of competing magnetic and electronic interactions that are responsible for anomalous low temperature thermodynamic and transport properties, thus playing an essential role in elucidation of physical properties [44]. RXS could therefore be an ideal technique to be combined with hydrostatic pressure in order to determine structural and electronic order parameters as a function of bond lengths. The scattering geometry for the pressure set-up on ID20 is unique with respect to other high pressure devices, since scattering occurs via a Beryllium gasket, which is highly transparent to X-rays in the energy range exploited for RXS, and the sample scattering surface is limited to $100 \times 300\ \mu m^2$ [45]. Fig. 7 shows recent experimental achievements in the detection of the small resonant magnetic signal at the Ce L_3-edge in 10% doped $CeFe_2$ [46]. These first results are encouraging and show clearly the feasibility of this technique, opening a large field of applications where low-temperatures and low energies are required, as for most of resonant and absorption spectroscopies [47].

5. Conclusions and perspectives

The knowledge of electric and magnetic multipoles of both parities under space-inversion and time-reversal can be of great importance in the understanding of the physics of strongly correlated electron systems, and their investigation has been a common theme of research during the last 20 years. In the light of this interpretation, the RXS technique can be applied to the investigation of many complex materials, such as Mott insulators, colossal magnetoresistive materials, actinides, high-Tc superconductors, multiferroics, heavy fermions and other transition metal oxides, in which orbital or multi-polar hidden order parameters coexist and influence the phase transitions [49–52].

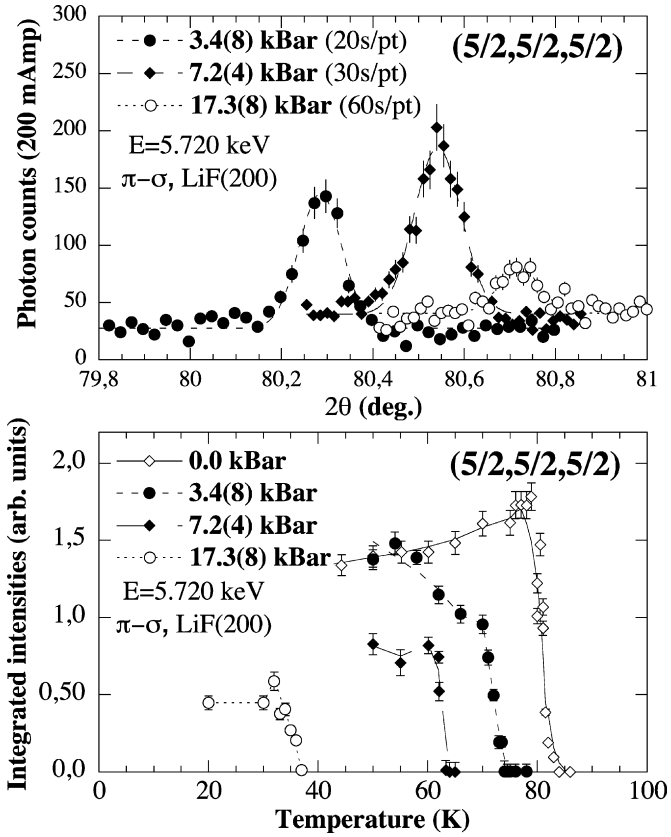

Fig. 7. High pressure RMXS experiments on $Ce(Co_{0.1}Fe_{0.9})_2$. Top: Antiferromagnetic reflection $(\frac{5}{2}, \frac{5}{2}, \frac{5}{2})$ taken at low temperatures at Ce L_3-edge ($E = 5.720$ keV) in π–σ' polarization channel. Bottom: Temperature dependence of $(\frac{5}{2}, \frac{5}{2}, \frac{5}{2})$ at different pressures (from Ref. [46]).

Fig. 7. Expérience à haute pression de diffraction magnétique résonnante des rayons X sur $Ce(Co_{0,1}Fe_{0,9})_2$. En haut : réflexion antiferromagnétique $(\frac{5}{2},\frac{5}{2},\frac{5}{2})$ à basse température au seuil Ce L_3 dans le canal depolarisation π–σ'. En bas : dépendance en temperature de la réflexion antiferromagnétique $(\frac{5}{2},\frac{5}{2},\frac{5}{2})$ à différentes pressions (d'après [46]).

The azimuthal dependence is a method which directly measures the symmetries of the tensors involved in resonant scattering amplitudes by measuring the diffracted X-ray linear polarization upon rotating the sample around the scattering vector. This technique has been essential in a number of high-profile cases, as for example the orbital ordering in transition metals [17,27,53], charge ordering and metal-insulator transitions [54,55], frustrated magnetism in low-dimensional systems [56] or induced magnetism in non-magnetic elements [57]. The azimuthal dependence can also be used to discriminate the magnetic domain populations in the non-resonant X-rays scattering regime, in order to determine the ratio between the ordered orbital and spin magnetic moment as well as their reciprocal directions [25,26,58]. Interesting Physics can also be addressed in multi-k antiferromagnets in which quadrupolar and magneto-vibrational interactions are far from negligible [59,60].

The possibility to control the incident beam polarization by diamond phase plates and to analyze the polarization of the scattered photons as a function of the azimuthal scattering geometry and the incident energy will play an important role in the future of this technique, providing a way to obtain information on the symmetry of the ordered structure when several multipole interactions close in energy contribute to the same transition [41].

High magnetic fields, pressures and low temperatures are fundamental parameters to study complex phase transitions and to disentangle competing electronic interactions in advanced materials. The development of extreme conditions in RXS will provide new powerful tools for investigating quantum phase transitions and the peculiar electronic behavior of strongly correlated electron systems.

Acknowledgements

All the coworkers in the experimental studies presented above are acknowledged, in particular the ID20 beamline team at ESRF. We would like to acknowledge R. Caciuffo and S. Di Matteo for useful discussions.

References

[1] D. Gibbs, J.P. Hill, C. Vettier, New directions in X-ray magnetic scattering, in: D.M. Mills (Ed.), Third-Generation Hard X-Ray Synchrotron Radiation Sources: Source Properties, Optics, and Experimental Techniques, John Wiley & Sons, Inc., 2002, pp. 267–310.
[2] M. Blume, J. Appl. Phys. 57 (1985) 3615–3618.
[3] D. Gibbs, D.R. Harshman, E.D. Isaacs, D.B. McWhan, D. Mills, C. Vettier, Phys. Rev. Lett. 61 (1988) 1241–1244.
[4] O. Klein, Y. Nishina, Zeit. Phys. 52 (1929) 853–868;
Y. Nishina, Zeit. Phys. 52 (1929) 869–877.
[5] A.H. Compton, Phys. Rev. 50 (1936) 878–881.
[6] M. Gell-Mann, M.J. Goldberger, Phys. Rev. 96 (1954) 1433–1438.
[7] F.E. Low, Phys. Rev. 96 (1954) 1428–1432.
[8] H.A. Tolhoek, Rev. Mod. Phys. 28 (1956) 277–298.
[9] F. de Bergevin, M. Brunel, Phys. Lett. A 39 (1972) 141–142.
[10] P.M. Platzman, N. Tzoar, Phys. Rev. B 2 (1970) 3556–3559.
[11] F. de Bergevin, M. Brunel, Acta Cryst. A 37 (1981) 314–331;
F. de Bergevin, M. Brunel, Acta Cryst. A 37 (1981) 324–331.
[12] L.K. Templeton, D.H. Templeton, R. Phizackerley, R.P. Hodgson, Acta Cryst. A 38 (1982) 74–78.
[13] V.E. Dmitrienko, Acta Cryst. A 39 (1983) 29–35.
[14] K. Namikawa, M. Ando, T. Nakajima, H. Kawata, J. Phys. Soc. Japan 54 (1985) 4099–4102.
[15] J.P. Hannon, G.T. Trammel, M. Blume, D. Gibbs, Phys. Rev. Lett. 61 (1988) 1245–1248.
[16] C. Vettier, J. Elect. Spectr. Rel. Phen. 117–118 (2001) 113–128.
[17] L. Paolasini, C. Vettier, F. de Bergevin, F. Yakhou, D. Mannix, A. Stunault, W. Neubeck, M. Altarelli, M. Fabrizio, P.A. Metcalf, J.M. Honig, Phys. Rev. Lett. 82 (1999) 4719–4722.
[18] Y. Joly, S. Di Matteo, C.R. Natoli, Phys. Rev. B 69 (2004) 224401 (1–11).
[19] S. Loversey, J. Fernández-Rodríguez, J.A. Blanco, D.S. Sivia, K.S. Knight, L. Paolasini, Phys. Rev. B 75 (2007) 014409 (1–8).
[20] I. Marri, P. Carra, Phys. Rev. B 69 (2004) 113101 (1–4).
[21] S. Di Matteo, Y. Joly, C.R. Natoli, Phys. Rev. B 72 (2005) 144406 (1–6).
[22] S. Loversey, E. Balcar, K.S. Knight, J. Fernández-Rodríguez, Phys. Rep. 411 (2005) 233–289.
[23] M. Blume, Resonant anomalous X-ray scattering, in: G. Materlik, J. Sparks, K. Fisher (Eds.), Elsevier Science B.V., Amsterdam, 1994, pp. 495–512.
[24] V. Fernandez, C. Vettier, F. de Bergevin, C. Giles, W. Neubeck, Phys. Rev. B 57 (1998) 7870–7876.
[25] W. Neubeck, C. Vettier, F. de Bergevin, F. Yakhou, D. Mannix, L. Ranno, T. Chatterji, J. Phys. Chem. Solids 62 (2001) 2173–2180.
[26] S.L. Langridge, G.H. Lander, N. Bernhoeft, A. Stunault, C. Vettier, G. Grübel, C. Sutter, F. de Bergevin, W.J. Nuttall, W.G. Stirling, K. Mattenberger, O. Vogt, Phys. Rev. B 55 (1997) 6392–6398.
[27] R. Caciuffo, L. Paolasini, A. Sollier, P. Ghigna, E. Pavarini, J. van der Brink, M. Altarelli, Phys. Rev. B 65 (2002) 174425 (1–9).
[28] M.T. Hutchings, E.J. Samuelsen, G. Shirane, K. Hirakawa, Phys. Rev. 188 (1969) 919–923.
[29] D. Mannix, P.C. de Camargo, C. Giles, A.J.A. de Oliveira, F. Yokaichiya, C. Vettier, Europ. Phys. J. B 20 (2001) 19–25.
[30] E. Kravtsov, A. Nefedov, F. Radu, A. Remhof, H. Zabel, R. Brucas, B. Hjörvarsson, A. Hoser, S.B. Wilkins, Phys. Rev. B 70 (2004) 054425 (1–8).
[31] M.R. Barbier, C. Mocuta, W. Neubeck, M. Mulazzi, F. Yakhou, K. Chesnel, A. Sollier, C. Vettier, F. de Bergevin, Phys. Rev. Lett. 93 (2004) 257208 (1–4).
[32] V.M. Dubovik, V.V. Tugushev, Phys. Rep. 187 (1990) 145–202.
[33] J.L. Rubin, Nuovo Cimento 15 (1993) 59–72.
[34] L. Paolasini, S. Di Matteo, C. Vettier, F. de Bergevin, A. Sollier, W. Neubeck, F. Yakhou, P.A. Metcalf, J.M. Honig, J. Electron. Spectrosc. Relat. Phenom. 120 (2001) 1–10.
[35] K.D. Finkelstein, Q. Shen, S. Shastri, Phys. Rev. Lett. 69 (1992) 1612–1615.
[36] P. Carra, B.T. Thole, Rev. Mod. Phys. 66 (1994) 1509–1515.
[37] S. Di Matteo, Y. Joly, A. Bombardi, L. Paolasini, F. de Bergevin, C.R. Natoli, Phys. Rev. Lett. 91 (2003) 257402 (1–4).
[38] Y. Murakami, H. Kawada, H. Kawata, M. Tanaka, T. Arima, Y. Moritomo, Y. Tokura, Phys. Rev. Lett. 80 (1998) 1932–1935.
[39] R.M. Moon, Phys. Rev. Lett. 25 (1970) 527–529.
[40] Y. Joly, Phys. Rev. B 63 (2001) 125120 (1–11).
[41] C. Mazzoli, S.B. Wilkins, S. Di Matteo, B. Detlefs, C. Detlefs, V. Scagnoli, L. Paolasini, P. Ghigna, Phys. Rev. B, Rapid Comm. (2007), submitted for publication.
[42] L. Paolasini, C. Detlefs, C. Mazzoli, S. Wilkins, P.P. Deen, A. Bombardi, N. Kernavanois, F. de Bergevin, F. Yakhou, J.-P. Valade, I. Breslavetz, A. Fondacaro, G. Pepellin, P. Bernard, J. Synchrotron Rad. 14 (2007) 301–312.

[43] D. Mannix, D.F. McMorrow, R.A. Ewings, A.T. Boothroyd, D. Prabhakaran, Y. Joly, B. Janousova, C. Mazzoli, L. Paolasini, S.B. Wilkins, Phys. Rev. B (2007), submitted for publication.
[44] M. d'Astuto, A. Barla, N. Kernavanois, J.-P. Rueff, F. Baudelet, R. Rüffer, L. Paolasini, B. Couzinet, in: Lecture Notes in Physics, vol. 697, 2006, pp. 375–399.
[45] N. Kernavanois, P. Deen, D. Braithwaite, L. Paolasini, Rev. Sci. Instrum. 76 (2005) 083909 (1–5).
[46] D. Braithwaite, L. Paolasini, P.P. Deen, N. Kernavanois, F. Yakhou, P. Canfield, G. Lapertot, Phys. B: Cond. Matter 378–380 (2006) 782–783.
[47] P.P. Deen, D. Braithwaite, N. Kernavanois, L. Paolasini, S. Raymond, A. Barla, G. Lapertot, J.-P. Sanchez, Phys. Rev. B 71 (2005) 245118 (1–5).
[48] L. Paolasini, B. Ouladdiaf, N. Bernhhoeft, J.-P. Sanchez, P. Vulliet, G.H. Lander, P. Canfield, Phys. Rev. Lett. 90 (2003) 057201 (1–4).
[49] J.A. Paixão, C. Detlefs, M. Longfield, R. Caciuffo, P. Santini, N. Bernhoeft, J. Rebizant, G.H. Lander, Phys. Rev. Lett. 89 (2002) 187202 (1–4).
[50] S.B. Wilkins, J.A. Paixão, R. Caciuffo, P. Javorsky, F. Wastin, J. Rebizant, C. Detlefs, N. Bernhoeft, P. Santini, G.H. Lander, Phys. Rev. B 70 (2004) 214402 (1–9).
[51] S.B. Wilkins, R. Caciuffo, C. Detlefs, J. Rebizant, E. Colineau, F. Wastin, G.H. Lander, Phys. Rev. B 73 (2006) 060406(R) (1–4).
[52] H.C. Walker, K.A. McEwen, D.F. McMorrow, S.B. Wilkins, F. Wastin, E. Colineau, D. Fort, Phys. Rev. Lett. 97 (2006) 137203 (1–4).
[53] G. Subias, J. García, P. Berau, M. Neuriva, M.C. Sánchez, J.C. García Muñoz, Phys. Rev. B 73 (2006) 205107 (1–13).
[54] U. Staub, G.I. Meijer, F. Fauth, R. Allenspach, G. Bednorz, J. Karpinski, S. Kazakov, L. Paolasini, F. d'Acapito, Phys. Rev. Lett. 88 (2002) 126402 (1–4).
[55] V. Scagnoli, U. Staub, M. Janoush, A.M. Mulders, M. Shi, G.I. Meijer, S. Rosenkranz, S.B. Wilkins, L. Paolasini, S.W. Lovesey, Phys. Rev. B 72 (2005) 155111 (1–7).
[56] A. Bombardi, J. Rodriguez-Carvajal, S. Di Matteo, F. de Bergevin, L. Paolasini, P. Carretta, P. Millet, R. Caciuffo, Phys. Rev. Lett. 93 (2004) 027202 (1–4).
[57] D. Mannix, A. Stunault, N. Bernhoeft, L. Paolasini, G.H. Lander, C. Vettier, F. de Bergevin, D. Kaczorowski, A. Czopnik, Phys. Rev. Lett. 86 (2001) 4128–4131.
[58] A. Stunault, S. Soriano, T. Gourieux, C. Detlefs, C. Dufour, K. Dumesnil, J. Magn. Magn. Mat. 272–276 (2004) 546–548.
[59] M.J. Longfield, J.A. Paixão, N. Bernhoeft, G.H. Lander, Phys. Rev. B 66 (2002) 054417 (1–7).
[60] N. Bernhoeft, J.A. Paixão, C. Detlefs, S.B. Wilkins, P. Javorsky, E. Blackburne, G.H. Lander, Phys. Rev. B 69 (2004) 174415 (1–5).